JULIUS-MAXIMILIANS-UNIVERSITÄT-WÜRZBURG

BACHELOR THESIS

An approach to the 3D-Morphology of PKS 2155−304 on parsec to kilo-parsec scale

Author:
Michael Seeg

Supervisor:
Prof. Dr. Matthias Kadler

ASTRO WÜRZBURG

A thesis submitted in fulfilment of the requirements
for the degree of Bachelor of Science

in the group of

Prof. Dr. Matthias Kadler
Department for Astrophysics

Contents

Zusammenfassung

In dieser Bachelorarbeit werden Observationen verschiedener Frequenzen im Radio Bereich genutzt um die dreidimensionalen Struktur des Blazars PKS 2155−304 betrachten zu können. Da durch die Entfernung zu den beobachteten Objekten bei den Messungen alle Information über die Tiefenstruktur des Objektes verloren geht, kann der Ort der Emissionen nur in einem zweidimensionalen Bild senkrecht zur Sichtline ermittelt werden. Da die unterschiedlichen Frequenzen Aufschluss über den emittierten Energiebereich und damit auch der Nähe zum Kern, einem supermassiven schwarzen Loch, geben, kann man diese Informationen nuthen um Rückschlüsse auf die dreidimensionale Struktur zu ziehen. Das bedeutet für weniger energetische Regionen und damit den entschleunigten Teilchen eine weitere Entfernung zum Kern und für hoch energetische eine dementsprechend kürzere Entfernung. Um einen dreidimensionalen Aufbau des Blazars und seiner Emissionen zu erklären, müssen ebenfalls die Emissionen beider Jets voneinander unterschieden werden.

In dieser Arbeit wird ein neues 1.4 GHz-Bild des GMRT-Datenarchivs von 2005 präsentiert. Der Hauptteil der Arbeit geht um die Kalibration der Rohdaten sowie der Anwendung von CLEAN-Algorithmen und Selbstkalibration die zur Enstehung des Bildes angewendet werden, um es für eine Gegenüberstellung mit Daten aus anderen Frequenzen von 235 MHz, 610 MHz, 4.8 GHz und 8.4 GHz zu verwenden. In Bezug auf PKS 2155−304 konnten die einzelnen Strukturen, die in den Bildern zu sehen waren, zuerst nicht direkt einander zugewiesen werden, da sich die Richtung der Emissionen und deren Ausprägung stark unterscheiden. Das 1.4 GHz Bild ist hierbei eine Synthese der observierten Radio-Frequenzen. Diese zeigen zwei Jets in unterschiedliche Richtung bei kleineren Frequenzen und bei höheren Frequenzen, nur einen Jet. Es zeigt einen Jet in nordwestlicher Richtung und diffuse Emission in östliche die zum zweiten Jet gehören kann. Zwei Jets können auch in einem Bild vom VLA derselben Frequenz gesehen werden, jedoch ist die Auflösung in diesem geringer und ermöglicht keine Unterscheidung einer Jet Komponente oder diffuser Emission. Des Weiteren zeigen die Bilder der höheren Frequenzen einen Jet in entgegengesetzer Richtung zum GMRT Bild. Eine Erklärungsmöglichkeit ist eine Richtungsänderung des Jets je weiter er sich vom Kern entfernt. Was diesen die Sichtline kreuzen lässt und damit die gesamten Bilder in eine dreidimensionale Struktur des Jets einordnen lässt.

Abschließend wird aus dem 1.4 GHz-GMRT-Bild der Öffnungwinkel ermittelt und der Sichtwinkel mit einem einfachen Modell eingeschränkt. Daraus resultierend kann mit einem geeigneten Kosmologischen Model auf die Ausdehnung der Jet Strukturen im generierten Bild geschlossen werden.

Abstract

In this bachelor thesis several observations at different radio frequencies are used to reveal a three-dimensional projection on the blazar PKS 2155−304. The information of each image only contains a two-dimensional view of all emissions in the line of sight and all about the depth where it is emitted is lost. By comparing the images, the different energies of emissions and their region near the core, a super-massive black hole, of the blazar can be revealed and by using this information for generating the three-dimensional structure. For higher frequencies it is expected to see the more energetic regions near the core. Vice versa, for lower frequencies the outer, less energetic, more decelerated regions. To get a three-dimensional view of the blazar, emissions of the jet to the line of sight and its counter-jet need to be distinguished.

In his work a new 1.4 GHz-image from the GMRT data archive from 2005 is presented. The main emphasis is on the calibration with the program AIPS and analysing the different wavelengths. By applying the CLEAN-algorithm and self-calibration this image could be generated and is then used for the comparison with the frequencies 235 MHz, 610 MHz, 4.8 GHz and 8.4 GHz. For PKS 2155−304 it proved difficult to make a direct distinction because the structure and direction of the jet emerging from the black hole changed from lower to higher frequencies. The 1.4 GHz image provides a synthesis of the case of two jets for the lower frequencies and one jet for higher frequencies by showing a prominent jet like structure to the North-West and diffuse emission to the East indicating the second jet. This can be seen in an 1.4 GHz image of the VLA with lower resolution too but in this image the difference in the structure of the emission can not be seen. For the higher frequencies the jet changed to the opposite direction. A bending of a jet could explain this differences in the frequencies quite well and allows the view of the third dimension on this object.

Furthermore the opening angle of the jet can be measured and allows to constrain the inclination angle. By use of this angle together with a possible cosmological model and the distances in the 1.4 GHz-image from the GMRT, an idea of the whole structure of the emission and its extension can be given.

Chapter 1

Active Galactic Nuclei

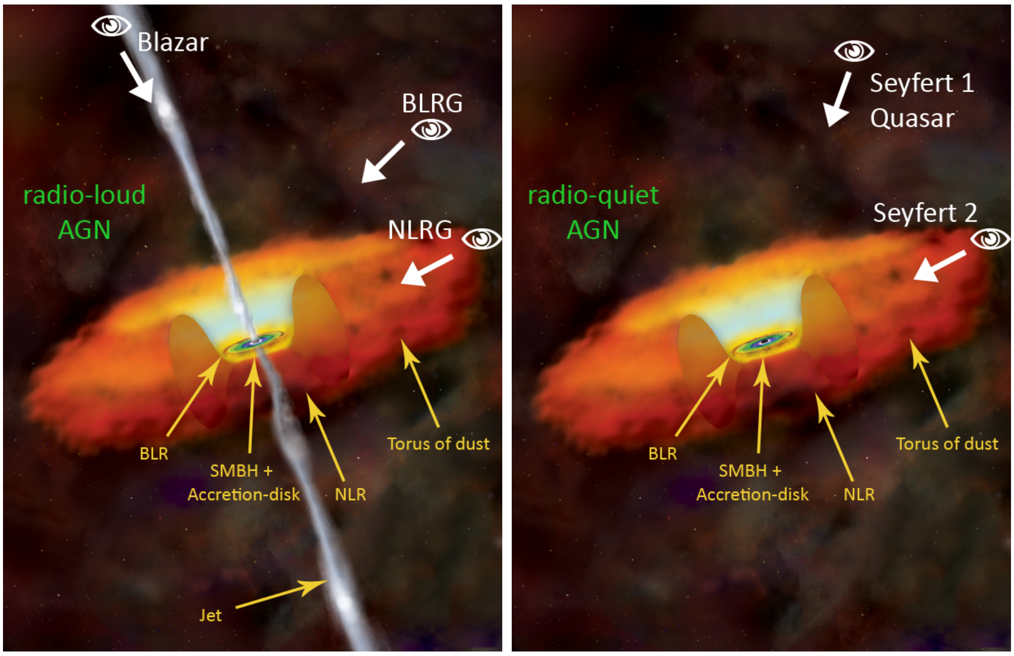

(a) Radio loud AGN

(b) Radio quiet AGN

Figure 1.1: The different types of AGN presented in this figure, illustrating the unified model. To the left the radio loud AGN are shown. Usually only they show a jet structure emerging from the black hole in the middle. The super-massive black hole is surrounded by an accretion disk and if seen, broad emission lines due to the doppler effect can be observed, they are then called Broad Line Radio Galaxies (BLRG) or Seyfert 1 for the radio quiet counter-part. If this Broad line region (BLR) is shielded by a torus of dust due to free-free absorption the AGN only shows narrow lines, therefore Narrow Line Radio Galaxies (NLRG) or Seyfert 2. This means the same Object is seen at different inclination angles and different features can observed.

AGN are compact objects with very high luminosities(Urry & Padovani 1995), in the region approximately $10^{4}2\,\frac{erg}{s}$ to $10^{4}7\,\frac{erg}{s}$. If everything of the structure of the AGN could be seen simultaneously we would expect a massive object, a black hole, with an accretion disk around it. Instead of nuclear fusion in stars, this is said to most probably come due to the accretion of mass onto a black hole. While the black hole is accumulating the mass of the disk, its potential energy is transformed into other kinds of energies, dependent on the accretion rate. This results in higher luminosities for a higher rate. A good explanation about the accretion and the resulting luminosities gives Shakura & Sunyaev (1973). The processes behind the high energy output can be observed in different wavelengths and with different imaging processes. By collecting data of all the wavelengths like optical, radio, x-ray and gamma information about the energies, locations, appearance, expansion and possible types can be gathered.

One attempt to get all the types of AGN into an order was made by Antonucci (1993) who summarized known information and classification about AGN into a model, seen in fig. 1.1. This unified model for AGN referred to the variety found as the same object, just from a different line of sight. Apart from the distinction of radio loud, with a jet, and radio quiet AGN, without a jet, by Peacock et al. (1986), the line of sight is said to be the explanation for the varying types.

The distinction between radio loud and quiet comes from the ratio $R_{o,r}$ of optical flux L_o to the radio flux L_r observed (Kellermann et al. 1989), where

$$R_{o,r} = \frac{L_o}{L_r} = \begin{cases} \geq 10 \Rightarrow \text{radio loud} \\ < 10 \Rightarrow \text{radio quiet} \end{cases} , \tag{1.1}$$

defines the threshold.

Seyfert I and Seyfert II galaxies are radio quiet types and differ by their emission lines Peterson (1997). Seyfert 1 galaxies show very broad emission lines from very dense matter regions together with thin forbidden lines, which form spontaneously in less dense matter. Seyfert 2 too show forbidden lines and allowed lines but both are narrow and generated in the same region.

Blazars are categorized as radio loud. They are subdivided in BL Lacertae (BL Lac), quasars and optical violent variable quasars (OVV) and are a pole-on view of the AGN. They are characterized by a compact core structure that dominates the whole galaxy, high variability and polarized spectra. The high polarisation supports the conclusion that non-thermal emission processes like synchrotron emission are its cause. Where electrons which are accelerated and confined by a magnetic field emit radiation in form of a cone parallel to their trajectory path according to their changing velocity. For Blazars, the angle to the line of sight of the jet emission is supposed to be very small and when observed it is to be expected to see only a point like structure. BL Lac objects are interesting for different wavelengths in the radio regime for the great differences that can be observed at the core and around them, because low energy regions observable at low frequencies, called extended emissions, give insight to the morphology of the object

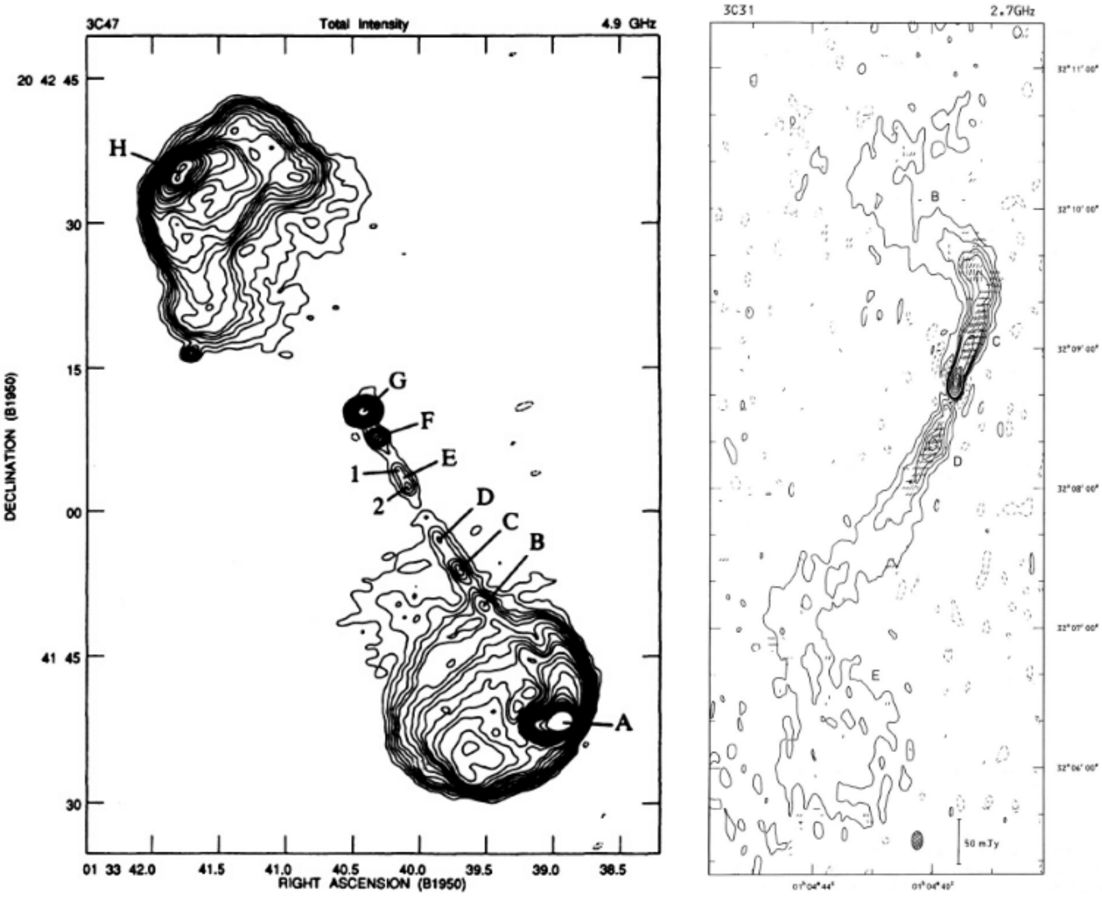

(a) FR2 galaxy

(b) FR1 galaxy

FIGURE 1.2: The different types of Fanaroff-Riley type galaxies. a) shows 3C47 (Bridle et al. 1994), a typical FR2 galaxy. It has two bright hot spots and a one sided jet. b) shows the object 3C31 (Burch 1979). This typical FR1 galaxy shows plumes emerging of both continuous jets.

far away from its core. While the high variability is promising for simultaneous multi-wavelength observations for the time relevant flares and therefore energy outbursts. The counterpart of Blazars in the unified model are radio galaxies which provide an edge-on view on the AGN. The general difference in this model is the luminosity. Fanaroff & Riley (1974) classified them into two types, the low luminosity FR1 type and high luminosity FR2 type galaxies. The extended luminosity of the different types can be calculated as,

$$\log(\mathrm{L_{ext}}) = \begin{cases} < 24 \Rightarrow \text{for FR1 galaxies} \\ > 26.5 \Rightarrow \text{for FR2 galaxies} \end{cases}, \tag{1.2}$$

for $\mathrm{L_{ext}}$ in $\left[\frac{W}{Hz}\right]$. Fanaroff-Riley galaxies also typically can be distinguished with respect to their morphology. FR1 galaxies typically feature a bright core with broad jets extending from it, terminating in so called plumes as seen in fig. 1.2 b). FR2 galaxies typically feature a bright core and a one sided jet terminating in lobes which often feature hot spots as seen in fig. 1.2 a). If the classification between different radio galaxies between FR1 and FR2 can be made then in the unified model the same can be applied on Blazar-type galaxies. This sorts BL Lacs to FR1 and the quasars to the FR2 types. For this the understanding of the extended emissions holds the key to investigate the outer jet emission, extended emission, where the jet gets optically thin.

Chapter 2

Radio Interferometry

The quantities measured for the observation of an object are visibilities, for this an understanding of electric fields (Clark 1999), of which only the quasi-monochromatic components can be measured, are explained first. For that, the use of a celestial plane at a convenient point between the observer and the observed or any radiating object is required. An interpretation of these field geometrics is shown in fig.2.1 a), it shows the emitted E-field at a distance $\vec{R}$ observed at point $\vec{r}$. It can be explained as follows.

The field,

$$\vec{E}_\nu(\vec{r}) = \int\int\int P_\nu(\vec{R},\vec{r})\vec{E}_\nu(\vec{R})dxdydz, \tag{2.1}$$

with $\vec{E}_\nu$ a monochromatic electric field at different locations and a green function P_ν as a propagator from source to observer, describes the influence of the field at point $\vec{r}$ by the field at $\vec{R}$. Note that the Field $\vec{E}_\nu$ here still is a vector field, which changes to a scalar field with the simplification of ignoring polarization phenomena. In radio astronomy due to the long distances of observing sources the image depth is lost. Therefore the measured quantity is a surface brightness distributed on a field of a celestial plane as seen in fig. 2.1 (b), where the projection of the fields on a celestial plane is shown. The field that will be observed now is the distribution of the field of the source on the surface of the sphere (ε_ν). Now the e-field written is a scalar and all depth information is lost by summarizing the e-field in line of sight to the celestial plane (ε_ν). With the distribution on this surface and the propagator, through an empty space, as a simple function, equation 2.1 concludes in,

$$E_\nu(\vec{r}) = \int \varepsilon_\nu(\vec{R})\frac{e^{2\pi i\nu|\vec{R}-\vec{r}|/c}}{|\vec{R}-\vec{r}|}dS, \tag{2.2}$$

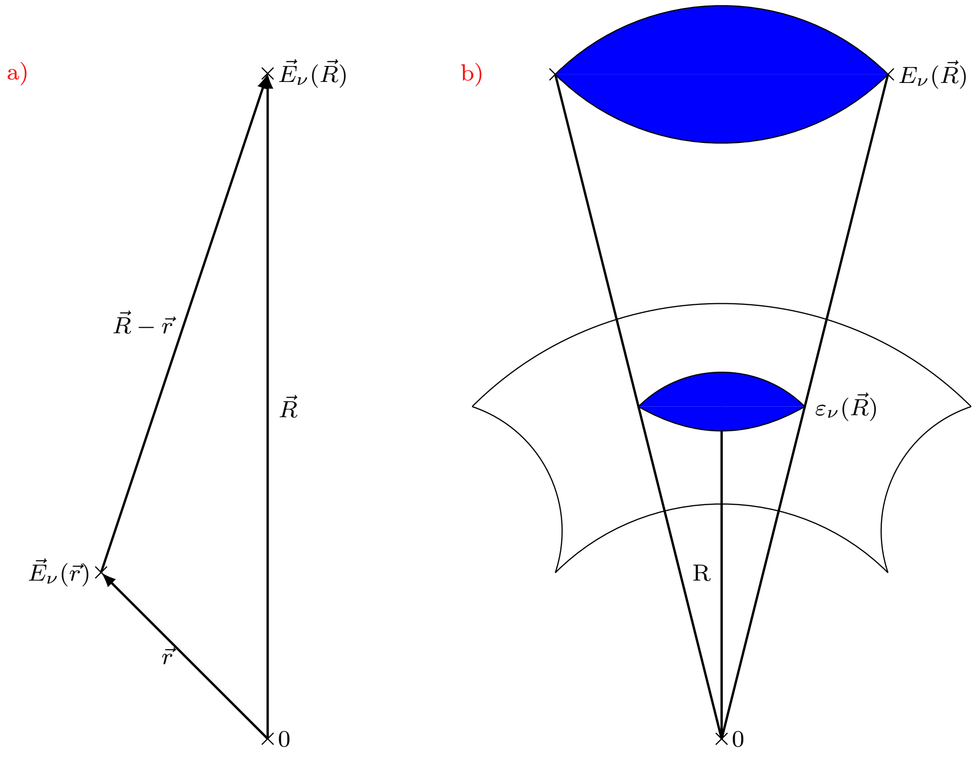

(a) $\vec{E}_\nu-$field geometrics

(b) $\vec{E}_\nu-$field projected on surface area

FIGURE 2.1: The $\vec{E}-$field for sources at a distance $\vec{R}$ with a) the distance of observer at $\vec{r}$ and superposition of locations, b) the field properties when all image depth is lost and the 2-dimensional source is projected on a surface area of a sphere. From Burd (2017).

with dS as a surface element, the speed of light c and the frequency ν. The interaction of a field when observed from two different locations is known and can be used for the expectation product, resulting in the cross correlation value $V_\nu = \langle \vec{E}_\nu(\vec{r}_1)\vec{E}^*_\nu(\vec{r}_2)\rangle$ with $\vec{E}_\nu(\vec{r}_2)$ complex conjugated, indicated with the Asterisk.

Writing the fields with the distribution of their field over the surface area of the celestial plane and using the assumption that these distributed fields expectation value for different locations is zero (results where $\frac{\vec{r}}{|\vec{R}|}$ can be neglected for great distances) the expectation value can be written as,

$$V_\nu(\vec{r}_1,\vec{r}_2) = \int \langle|\varepsilon_\nu(\vec{R})|^2\rangle|\vec{R}|^2 \frac{e^{2\pi i\nu|\vec{R}-\vec{r}_1/c}}{|\vec{R}-\vec{r}_1|}\frac{e^{-2\pi i\nu|\vec{R}-\vec{r}_2/c}}{|\vec{R}-\vec{r}_2|}dS. \tag{2.3}$$

Changing the equation to the unitvector $\vec{s}=\vec{R}/|\vec{R}|$, the surface element $\mathrm{dS} = |\vec{R}|^2 d\Omega$ and substituting $|\vec{R}|^2\langle|\varepsilon_\nu(\vec{s})|^2\rangle$ for the observed intensity $\mathrm{I}_\nu(\vec{s})$ gives the spacial coherence function,

$$V_\nu(\vec{r_1},\vec{r_2}) \approx \int I_\nu(\vec{s})e^{-2\pi i\nu\vec{s}(\vec{r}_1-\vec{r}_2)/c}d\Omega. \tag{2.4}$$

This is only a short introduction of Clark (1999). For a better understanding of the whole radio interferometry process I recommend reading a combined work about synthesis imaging compiled by Taylor et al. (1999).

An object with angular extension lower than the resolution of our telescope is worked with, it is therefore seen as a point source. Depending on the angle of observation and the characteristics (effective collecting area A(ν,Θ,Φ), response of the center of the main lobe A$_0$(m^2) and sensitivity) of the antenna, an image can be obtained via convolution with the brightness distribution (Napier 1999). The beam, which is dependent on the characteristics of the telescope, is a Fourier transformation of the aperture current density distribution.

Earth rotation synthesis is used to measure the brightness I$_\nu$ over time. The time of observation as crucial, it provides more necessary points in the Fourier-space, in radio astronomy called the (u,v)-plane, for the Fourier transformation. The more points in the (u,v)-plane, the better the recreation of the source by smoothing the fringes by the interacting electromagnetic waves observed (Thompson 1999) and therefore resolution should be related to the distance between a given point in the (u,v)-plane from the center. The point density should enhance the sensitivity. Each point is a measurement by telescopes at a distance with respect to the source, called a baseline b$_\lambda$. Meaning, with the locations of the telescopes a beam pattern is constructed with fixed points that change in time and the coherence function V_ν is only known for these samples. A detailed sketch of one Baseline can be seen in fig. 2.2. As a simplification the information about the baselines of the array is projected onto the uv-plane and setting in on the location of $w = 0$. The $\lambda(u,v,0)$ of $\vec{b}_\lambda$ is the spacing between two locations $(\vec{r_1}-\vec{r_2})$ on a plane perpendicular to the pointing vector, which can be described in the same coordinate system at the source with the unit vector $\vec{s} = (l, m, \sqrt{1-l^2-m^2})$. For which equation 2.4 is rewritten,

$$V_\nu(u,v,0) = \int\int I_\nu(l,m)\frac{e^{-2\pi i(ul+vm)}}{\sqrt{1-l^2-m^2}}\,dl\,dm. \tag{2.5}$$

for $\lambda =$ c/ ν, shows a Fourier transform relation which can be inverted. The unit vector $\vec{s}$ for a small region of the sky is used for another simplifying assumption. All radiation is coming only from a small proportion of the field observed. Our unit vector is therefore the same as a small deviation from it $\vec{s} = \vec{s}_0 + \sigma$ and this implies that our $\vec{s}_0$ and σ are

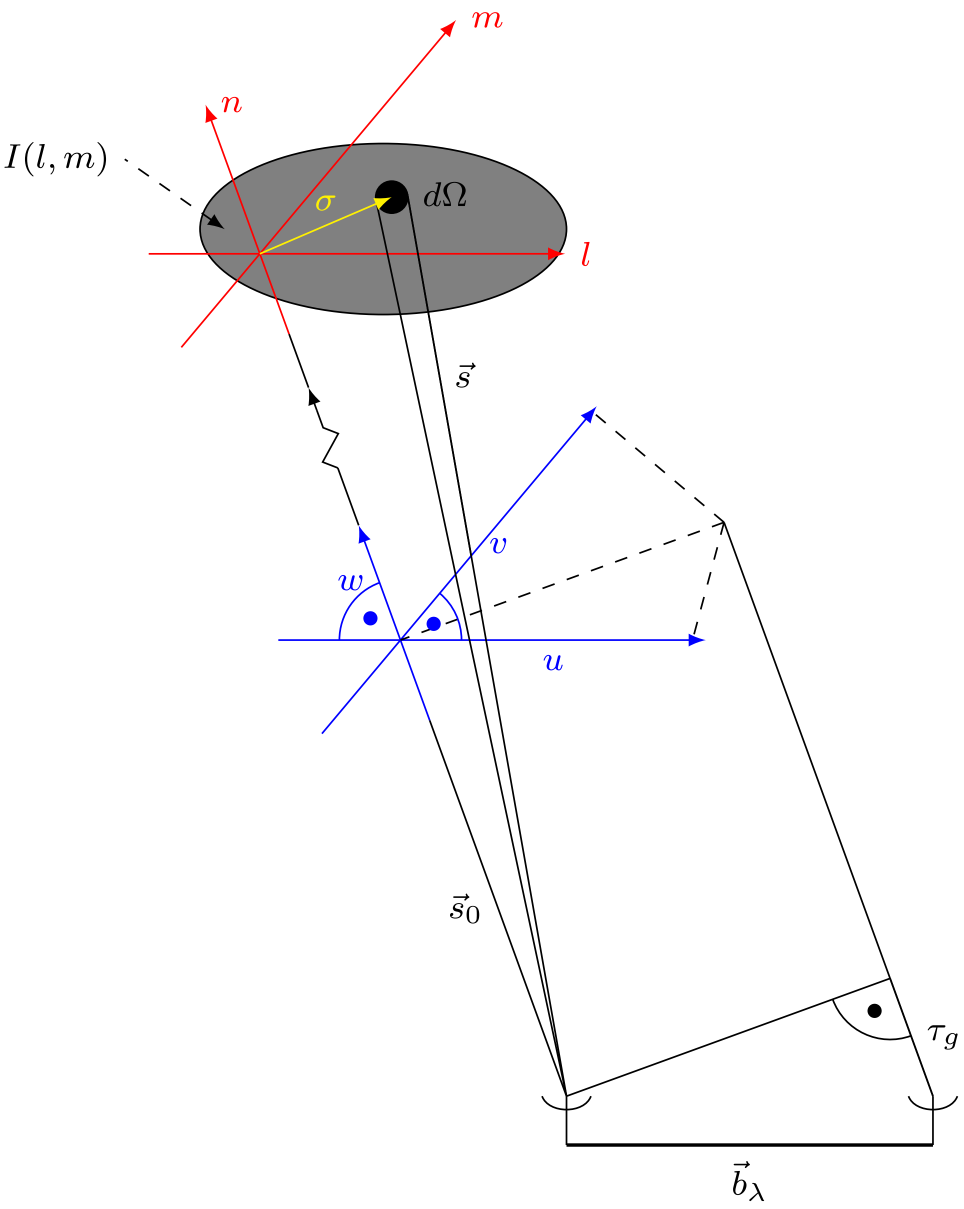

FIGURE 2.2: The baseline $\vec{b}_\lambda$ is dependent on the distance between the telescopes as seen here in a simplified sketch of two telescopes. The wave fronts arrive with a different delay τ_g at each telescope and the geometrical information is projected onto the (u,v)-plane (where w=0), for the Fourier transformation. $\vec{s}_0$ is the pointing vector and $\vec{s}$ the location of the target. These are separated by σ on the (l,m,)-plane (where n=0) with which the intensity I(l,m) is described. dΩ defines a small area on the plane. From Burd (2017).

perpendicular and the spacial coherence function is slightly different,

$$V'_\nu(u,v,w) = e^{-2\pi iw} \int\int I_\nu(l,m) e^{-2\pi i(ul+vm)}\, dl\, dm. \tag{2.6}$$

With $V_\nu = e^{-2\pi iw} V'_\nu$ a direct inversion of the spacial coherence function is accomplished,

$$I_\nu(l,m) = \int\int V_\nu(u,v,) e^{2\pi i(ul+vm)}\, du\, dv. \tag{2.7}$$

This assumption can only be made if both, the location of end points $\vec{s}$ and starting points $\vec{r}$, lie each on a plane parallel to each other, because this way they can be described by one vector to the plane and by the location on their plane.
Due to the sampled information of all the baselines a function S(u,v), that is set to zero for points were no data has been taken, is introduced and inserted in equation 2.7. This equation,

$$I_\nu * B = I^D_\nu(l,m) = \int\int V_\nu(u,v,) S(u,v) e^{2\pi i(ul+vm)}\, du\, dv. \tag{2.8}$$

is called the dirty image and via a convolution with the synthesised beam, also called point spread function in optics,

$$B(l,m) = \int\int S(u,v) e^{2\pi i(ul+vm)}\, du\, dv \tag{2.9}$$

it reverts back to equation 2.7. This equations would describe the reception pattern in a ideal sense for the telescopes. No effects by the receiving antenna would disturb the reception, but the sensibility for the pointed direction of the telescope differs for deviations (Clark 1999) and an additional factor in eq.2.6, here called $\mathcal{A}_\nu$, has to be introduced,

$$V_\nu(u,v) = \int\int \mathcal{A}_\nu(l,m) I_\nu(l,m) e^{-2\pi i(ul+vm)}\, dl\, dm, \tag{2.10}$$

finally described as the complex visibility relative to a phase tracking center. $\mathcal{A} = \mathsf{A}(\vec{\sigma})/\mathsf{A}_0$ is describing the primary beam of the telescope, a normalization of the antenna reception pattern $\mathrm{A}_{\vec{\sigma}}$ by its response at the beam center A_0 (Napier 1999). $\vec{\sigma}(l,m)$ is a vector on the plane of pointing vector $\vec{s}_0$ seen in fig.2.2.
Regarding to this, the unit Jansky

$$1\,[\,\mathsf{Jy}] = 10^{-26}\left[\frac{\mathsf{J}}{\mathsf{s\ m^2\ Hz}}\right] \tag{2.11}$$

is used, the energy per second on a square meter per hertz, as a better reference unit in radio astronomy used for the spectral power flux density. Equation 2.10, with $\vec{\sigma}$ and ν

over the entire surface S by small regions $d\Omega$ would result in

$$V_\nu = \int\limits_{\mathrm{S}} \mathcal{A}(\vec{\sigma}) I(\vec{\sigma}) e^{-2\pi i \nu \vec{b}\vec{\sigma})/c}\, d\Omega \tag{2.12}$$

Michelson (1890) first introduces visibilities, a measure for coherence, which gives the relative amplitude of the optical fringes. The visibilities in radio astronomy are complex quantities of coherence in an electric field measured without normalization in the dimension of Jansky and modified by the interferometer.

As mentioned in fig.2.2 a geometrical delay τ_{g} between two or an array of more telescopes needs to be accounted for. Depending on the length of the path difference the light has to travel, the time of arrival of the coherent electromagnetic waves at the telescope differs and can not be neglected. The information on the whole delay time between signals is crucial for interferometry and has to be well known. Not only geometrical but instrumental delays or atmospheric delays and the corrections have to be made for the process of further study by direct measuring or reference measurements explained in chapter 3. Using more than one telescope needs to put every signal measured together, whose delay was adjusted for each telescopes. A correlator merges the amplified signals for all baselines into a response function (Thompson 1999),

$$r(\tau_{\mathrm{g}}) = v_1\, v_2\, cos\, 2\pi\nu\tau_{\mathrm{g}}, \tag{2.13}$$

where v_1 and v_2 are the signals of the telescopes, τ_{g} is the geometrical delay and ν is the frequency of the observation. Actually the work of the correlator is much more complex, but for this bachelor thesis its description would go beyond its supposed length, a thorough description is given by Romney (1999).

As mentioned earlier in this section, the observed visibility $\tilde{V}_{\mathrm{ij}}(\mathrm{t})$ is different from the actual visibility V_{ij} but it is approximated that arrays are linear devices (Fomalont & Perley 1999). The baseline-based complex gain $\mathrm{G}_{\mathrm{ij}}(\mathrm{t})$ for two telescope pairs i and j with a complex offset $\epsilon_{\mathrm{ij}}(\mathrm{t})$ and a stochastic complex noise $\eta_{\mathrm{ij}}(\mathrm{t})$ allow that $\tilde{V}_{\mathrm{ij}}(\mathrm{t})$ can be written as,

$$\tilde{V}_{\mathrm{ij}}(t) = G_{\mathrm{ij}}(t) V_{\mathrm{ij}}(t) + \epsilon_{\mathrm{ij}} + \eta_{\mathrm{ij}}(t). \tag{2.14}$$

For calibration purposes the complex gain function needs to be approximated to the observed visibilities in order to represent the actual visibility $\mathrm{V}_{\mathrm{ij}}(\mathrm{t})$. A product of the two separate gain functions of the antennas of a baseline with information about their amplitude and phase allows that.

$$G_{\mathrm{ij}}(t) = g_{\mathrm{i}}(t) g_{\mathrm{j}}^{*}(t) = a_{\mathrm{i}}(t) a_{\mathrm{j}}(t) e^{i(\Phi_{\mathrm{i}}(t) - \Phi_{\mathrm{j}}(t))}, \tag{2.15}$$

has the information about the amplitude correction a(t) of each antenna and Φ(t), the antenna phase correction. These values can be obtained by calibrator sources, which will be explained in section 3.

Enhanced by the complex gain function the complex visibility can now be written as,

$$V_{\mathrm{ij}}(t) = \int\limits_{0}^{\infty} \left(\int\limits_{-\infty}^{\infty} \int\limits_{-\infty}^{\infty} \mathcal{A}_{\nu}(l,m) I_{\nu}(l,m) e^{-2\pi i(ul+vm)}\, dl\, dm \right) e^{2\pi i\nu\Delta\tau_{\mathrm{r}}} G_{\mathrm{ij}}\, d\nu, \tag{2.16}$$

where (i,j) denotes the antenna pair, ν is the frequency, $\mathrm{V_{ij}(t)}$ is the visibility function for a finite bandwidth, $\mathrm{G_{ij}}(\nu)$ the complex gain as a function of frequency and $\Delta\tau_{\mathrm{g}}$ as differential geometric delay relative to the tracking center and a residual instrumental delay $\Delta\tau_{\mathrm{r}}$ (Fomalont & Perley 1999). The complex gain is here a function of frequency because the gain is different for each wavelength observed. This also means that the whole bandwidth has to be calibrated in order to get a good approximation on the complex gain.

Chapter 3

Data Processing

The data received by the array of telescopes is not yet ready for physical interpretation. Though the amplitude and phase information from each dish is available and preprocessed, there is still calibrations to be done. As the data is collected from one source, there are still perturbations from the side-lobes, background radiation, errors in the alignment or power-fluctuations of each telescope. This can be seen in the dataset with all baselines and has to be corrected. Pollutions of the data are for example Radio Frequency Interference (RFI) and these need to be discarded to achieve a interpretable set of data for further processing. For this certain programs are used, like AIPS and Difmap. The program to calibrate the flux and phase with other sources is called AIPS. AIPS allows to calibrate the raw data by gauging it with sources, with thorough extensive observation and known physical properties, made in the same observation window to reduce perturbation. After receiving the ".fits" observation files from the GMRT database, they need to be implemented into AIPS. For this the file can simply be loaded into its own space in AIPS, called a port, in which it can be processed further. The file contains several informations about the sources observed, like locations and visibilities. This can be done with the task FITLD, which loads both maps and UV-data into a catalogue. AIPS works with extension files, all changes while calibrating are stored in these files and new versions are generated every time a change in a specific table/file is made. The most important extension files are for plots, history, slices, images, flagged data (FG), bandpass (BP), calibration (CL), solutions (SN), index (NX). The actual data is never changed and because all changes are stored in new tables, every time an error is made it is easy to restore the table of an earlier task.

To be able to work with the data it needs to get an index with the task INDXR that allows us to generated a NX table that indexes the uv data file for quick access to the sources and the time range. When this is accomplished, the sources, their locations, visibilities, observation time, frequency and more information are accessible.

For the source to be calibrated right there are certain requirements for our calibrator-sources. To be ensure the right flux is measured, a flux calibrator is essential. This is a source where the flux is postulated to be well known by a large number of independent observations (Perley & Butler 2013) and usually this is a bright object without fluctuation in its brightness to ensure a good ratio between Signal and the noise (SNR), often objects from the 3C-catalogue. A useful tool is the "List of VLA Calibrator" provided by the National Radio Astronomy Observatory (NRAO) where the up to date data from studies like Scaife & Heald (2012) for low frequency from $\approx 10 - 1400\,\mathrm{MHz}$, Perley & Butler (2013) for a flux density scale for frequencies between 1 GHz to 50 GHz and of specific objects like Cas A Baars et al. (1977) are presented. With this the absolute flux density scale of the source can be calibrated. As mentioned in Chapter 2 the gathered information by the telescopes is processed by correlators and include every signal the electronics of the telescopes send.

To account for all delays that could occur between the source and the telescopes, information about the contributors to the delay would be needed. The easier and doable

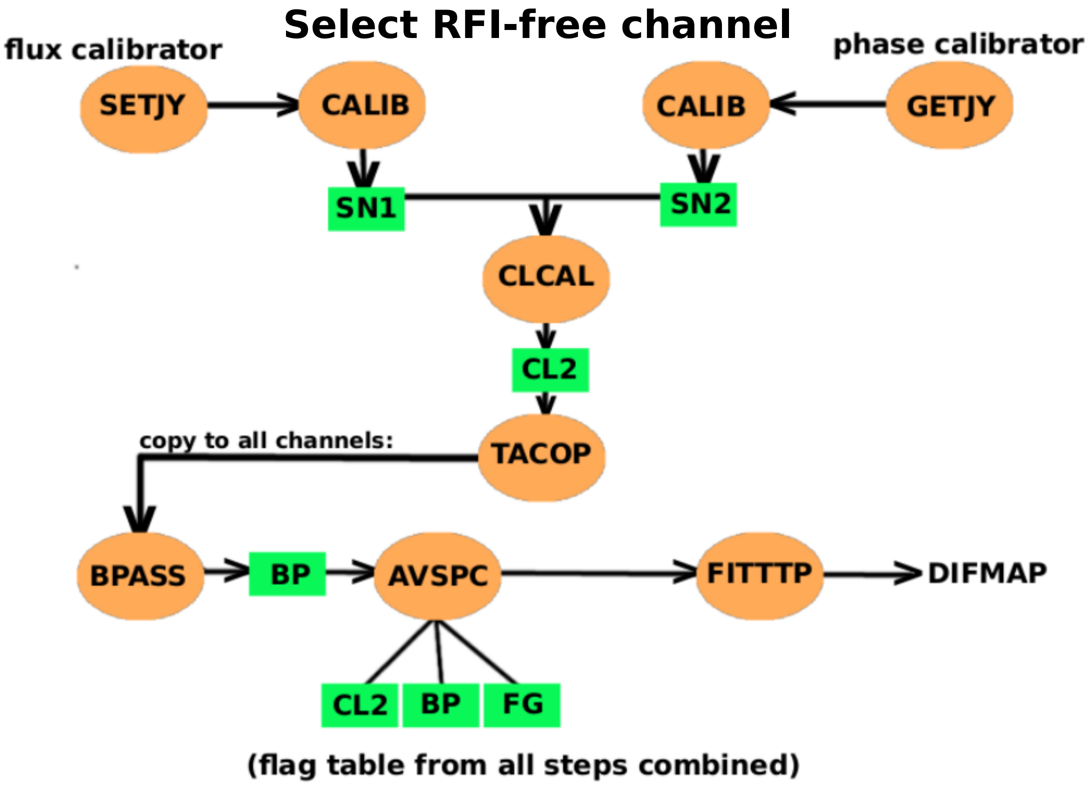

Figure 3.1: Simple sketch of steps of calibration process in AIPS. After separate calibration of one radio interference free channel by creating the solution tables for the flux and phase calibration those are merged and used for the calibration table. This table is then used on all channels together with a bandpass calibration table, which has to be applied too, to calibrate the different frequencies of the bandpass to each other.

way to get the overall delay is a phase calibrator source. The phase calibrator gives the information about the delay on the individual telescopes of the array. Ideally seen as a point source in the observation and the given resolution, the delays of the signal to each telescope differ. Due to the pointing angle of the telescopes, the path from source to the telescope-array may vary to each dish. Therefore another source needs to be observed that is stable in its wavelength to provide an estimate of the phase-shift of each dish. The effects of the instrumental delay can be measured with a good phase calibrator source, too. To calibrate the flux AIPS is equipped with information about the flux density of known flux calibrators, the source 3C48 for instance is one of them. The known information can be added to the observed flux calibrator by the task SETJY, adding it to the matching specific source into the SU table of the catalogue. With this option the flux density scale can be applied on the flux calibrator itself. With the task CALIB, the calibrator 3C48 can be checked and adjusted to its well known fluxes resulting in solutions obtained by the method of least square.

Due to RFI pollution, one RFI free channel is selected to perform the flux and phase calibration first to then apply it on the whole dataset. Therefore first the flux is calibrated to obtain the first solution-table (SN1) and then CALIB is used, which applies a point source model, to get the second solution-table (SN2) for the phase calibrator. With the solutions from the flux calibration the flux of the second SN-table can be scaled by GETJY. To finalise the calibration of the single channel both solutions table need to be merged into a calibration table (CL2) with the task CLCAL. This calibration table (CL2) is applied to the data of the source of interest and with it the calibration of the single channel is complete.

To calibrate the whole dataset and with it all channels it is necessary to perform a bandpass calibration. All channels have different amplitudes and phases and they need to be adjusted to correct leaps and slopes. A bandpass calibration is needed to minimize these variations of each channel to another. Each channel has a different gain function. It is not only dependent on the time but also on the frequency of each channel. With the bandpass calibration the gain function is adjusted to align the phases of all channels. If the bandpass is calibrated correctly the phase is now represented by a steady line. After the bandpass is calibrated, an averaged out version of the data is copied into a new catalogue via AVSPC, with all the flagged data (FG-table), if there is any, the bandpass-table (BP) and calibration table (CL2). With the task FITTP the data of a single source can then be extracted for the use in Difmap. This whole process can be seen in fig.3.1 as a simple sketch of the most important steps. DIFMAP's purpose is to work in a more user friendly program with the generated UV-fits files of programs like, AIPS or CASA (Shepherd 1997) with the use of special algorithms and the ability for self-calibration. With the visibilities of all baselines and the spacial frequency plane (fig.3.2) a dirty map can be generated with a fast fourier transform which is a product

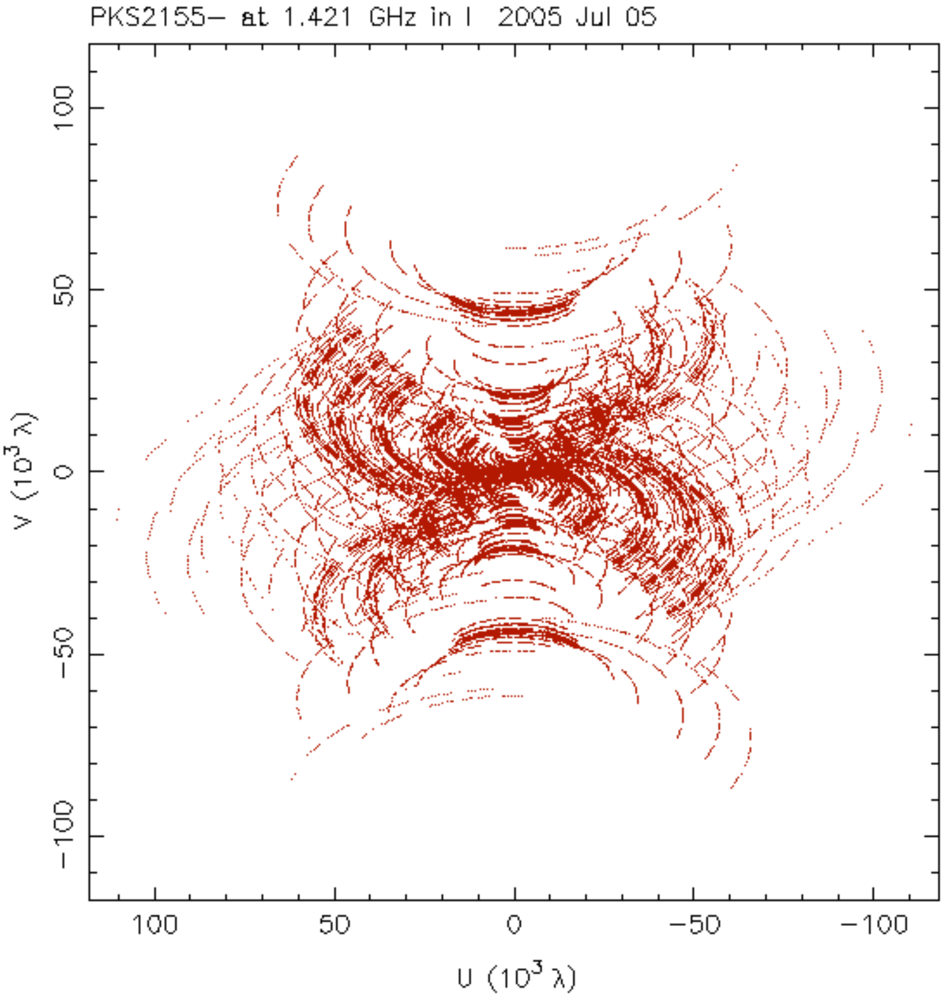

FIGURE 3.2: The UV-coverage from the GMRT of the Blazar PKS 2155−304 of an ≈7 h observation. For the Fourier transform this information is used in the convolution to produce a clean image. The longer the baseline the farther the visibility is away from the center. The concentrated area in the center shows the better coverage of the 1 km^2 field with 12 antennas. Dependent on the earth's rotation and angle to the object the Y-shaped form of the array progresses to a better coverage.

of the location of our telescopes and their instrumentally delayed complex wavefronts reaching their receivers.

The key in DIFMAP is the building of a model of the source which describes the data best. This is done by applying delta-functions to peaks in the dirty map and then subtracting the peak and a percentage of it from the whole dirty map resulting in a residual map, this is called a CLEAN-algorithm introduced by Högbom (1974). The algorithm assumes an image as a composition of point sources. Until the highest value is smaller than a threshold, it iteratively takes the higest value of the point sources to substract a small gain convolved with the dirty beam (point spread function) of the observation. Models can be added by selecting an area in which the highest peaks get a model component, or adding them manually. The command CLEAN is doing all that automatically in a desired location and even updates the residual map for further mapping of the source. By applying SELFCAL the amplitudes and phases can be corrected utilizing the closure relations, see Jennison (1958). The closure relations state that the phase between three telescopes is independent from antenna errors. This can be used to calibrate the data according to a given model by allowing each antenna phase and flux to change while letting the closure phase and flux unchanged. This method used together with CLEAN is called hybrid imaging. The goal is to rid the image of all interferences and artefacts to achieve a clean image without high noise obscuring the source observed.

Chapter 4

Multi-band analysis of PKS 2155−304 and 3D-structure

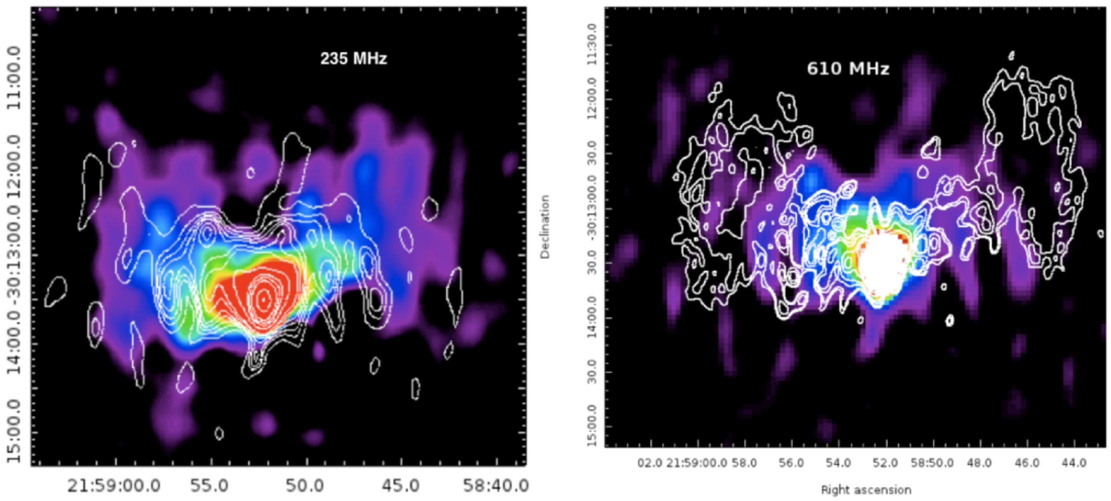

FIGURE 4.1: 325 Mhz view of PKS 2155−304 with a colour overlay of 610 Mhz and vice versa by (Pandey-Pommier et al. 2016). The beam size of the coloured background image has been adjusted to the resolution of the contour image. In both images the extended structure of the emission can be seen expanding to the East and West. The x-y-axis are both showing arc-minutes.

PKS 2155−304 is a BL Lac object, its locations is at 21h58m52.0651s (RA) -30d13m32.118s (DEC) at a redshift of 0.116 (Falomo et al. 1993). It is one of the brightest objects, especially in the TeV Band, in the southern hemisphere and it is known to be a highly variable Source (Chevalier et al. 2016). Most recent studies of this BL Lac object are for its flaring states like in the year 2006 by H.E.S.S. Collaboration et al. (2012) where the source showed energies up to 100 GeV and a multiwavelength study by Sanchez et al. (2015) for a SED from optical to TeV energies. With data from the GMRT after

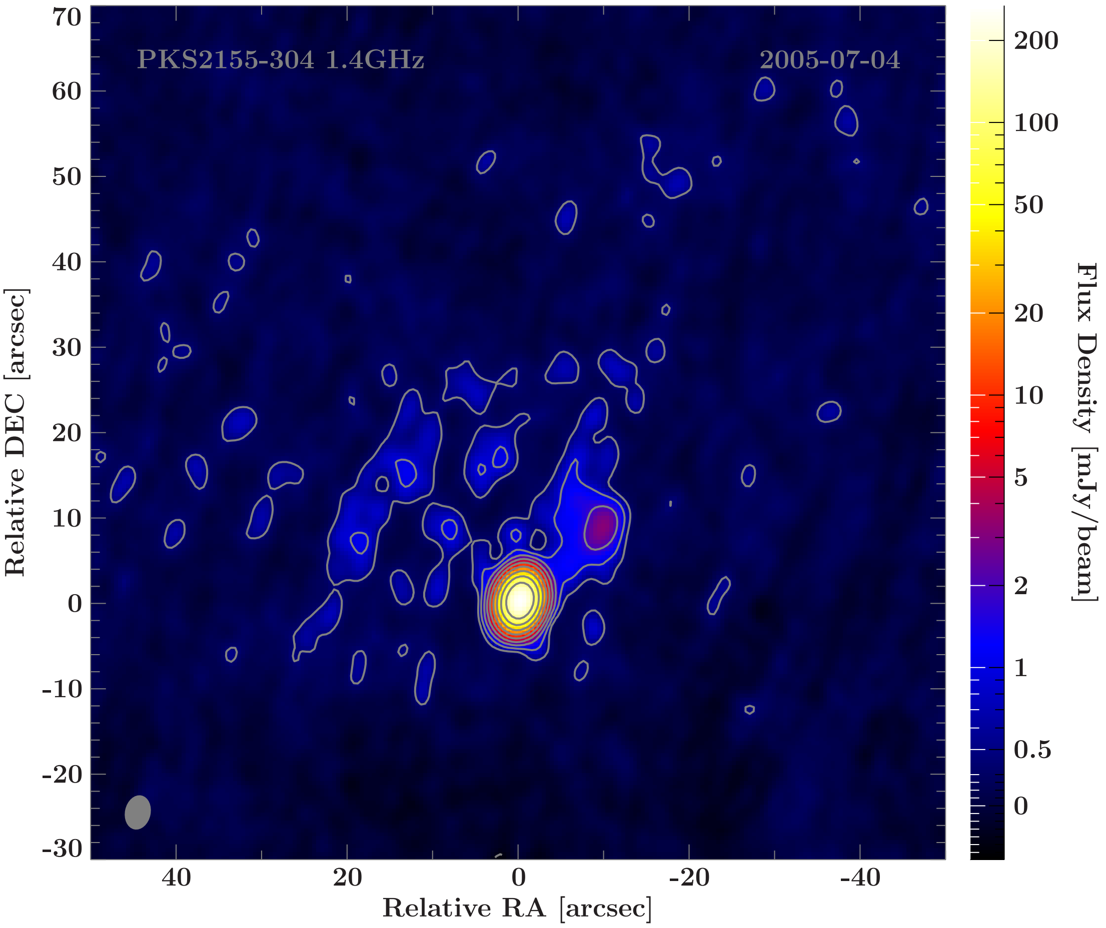

FIGURE 4.2: The 3-sigma image resulting from the calibration of the 1.4 GHz dataset from the GMRT-archive. A large jet like structure can be seen emerging from the core to the North-West with diffuse emissions all around the source but concentrated to the East. With a beam-size of (3.91 × 2.86) arcsec the overall flux in the image results in (0.438±0.044) Jy at a rms of 0.154 mJy. The contours are (-0.45, 0.45, 0.90, 1.80) mJy, show the 3 sigma threshold and are separated by a factor of 2^n for n as the number of the contour. The Error is about 10% after (Chandra et al. 2004). The flux of the core is (0.278±0.028) Jy.

the calibration process and imaging, Chapter 3, more information about the source in radio-wavelength at 1.4 Ghz could be achieved. In general this Blazar was subject to observations at different wavelengths already, for example by Pandey-Pommier et al. (2016) who produced two images, one at 325 Mhz and one at 610 Mhz, which were presented as overlaying images, seen in figure 4.1. The 1.4 Ghz image presented in their work is of lower resolution with (2 × 10) arcsec from Very Large Array (VLA) observation at 1.4 GHz and could not show the features near the core very well. This image was reproduced by data of the VLA archive and is presented in the upper left of fig. 4.5 together with a follow up observation at 4.8 GHz seen in the bottom. More recent studies about PKS 2155−304 with data from the VLA at different configurations provides Liuzzo et al. (2013), where jet like structures in Eastern and Norh-Western direction could be found.

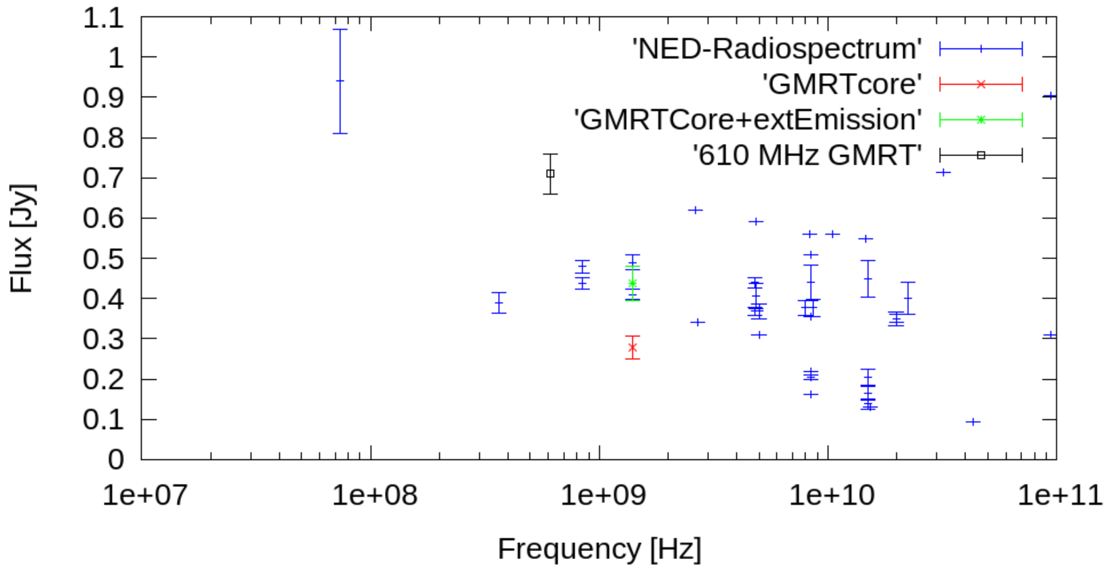

Figure 4.3: The radio-spectrum acquired from the NED-database with the flux acquired from the GMRT-image at 1.4 GHz. The flux obtained from the 1.4 GHz GMRT image is consistend with the overall radio spectrum. The core emissions are ≈ 0.15 Jy smaller. Additionally the flux of the 610 MHz lightcurve from Pandey-Pommier et al. (2016) has been added.

To investigate this further the new image from 2005 observed with the GMRT is used. After calibrating the raw GMRT-data with AIPS and imaging with the dirty image with Difmap a clean, high resolution image of PKS 2155−304 for further studying emerged. With a beam size of of (3.91 × 2.86) arcsec, with a position angle of P.A.=-12.1° the image at 1.421 GHz is higher resolved than the VLA-image used in (Pandey-Pommier et al. 2016). The image shows a bright core region with a flux of: $F_c = (0.278 \pm 0.028)$ Jy with a jet like structure to the north west and more concentrated but diffuse emissions to the East resulting in an overall flux of (0.438±0.044) Jy, the relative errors of the flux density is 10% (Chandra et al. 2004). It is shown in fig. 4.2. In comparison to the GMRT-images with the lower frequency images of Pandey-Pommier et al. (2016) the emissions emerging from the core differ with respect to the morphology. The GMRT-image shows a jet like emission only to the North-West with diffuse emission all around the core pointed to the East. Whereas in the images of (Pandey-Pommier et al. 2016) on both direction large structures at arc-minutes scales can be seen where the emission to the North-West is more collimated especially in the 610 MHz image. Also the flux of the 1.4 GHz image is in agreement with the NED-database, seen in fig. 4.3, if all emissions in it are added as a total flux. Therefore emissions only from the core are 0.15 Jy smaller and which is approximately the value for the flux of the extended emission. We would expect an increase of the extended emission which dominates the core emission for lower frequencies, but for this frequency this is not the case. Still, the flux is in agreement of

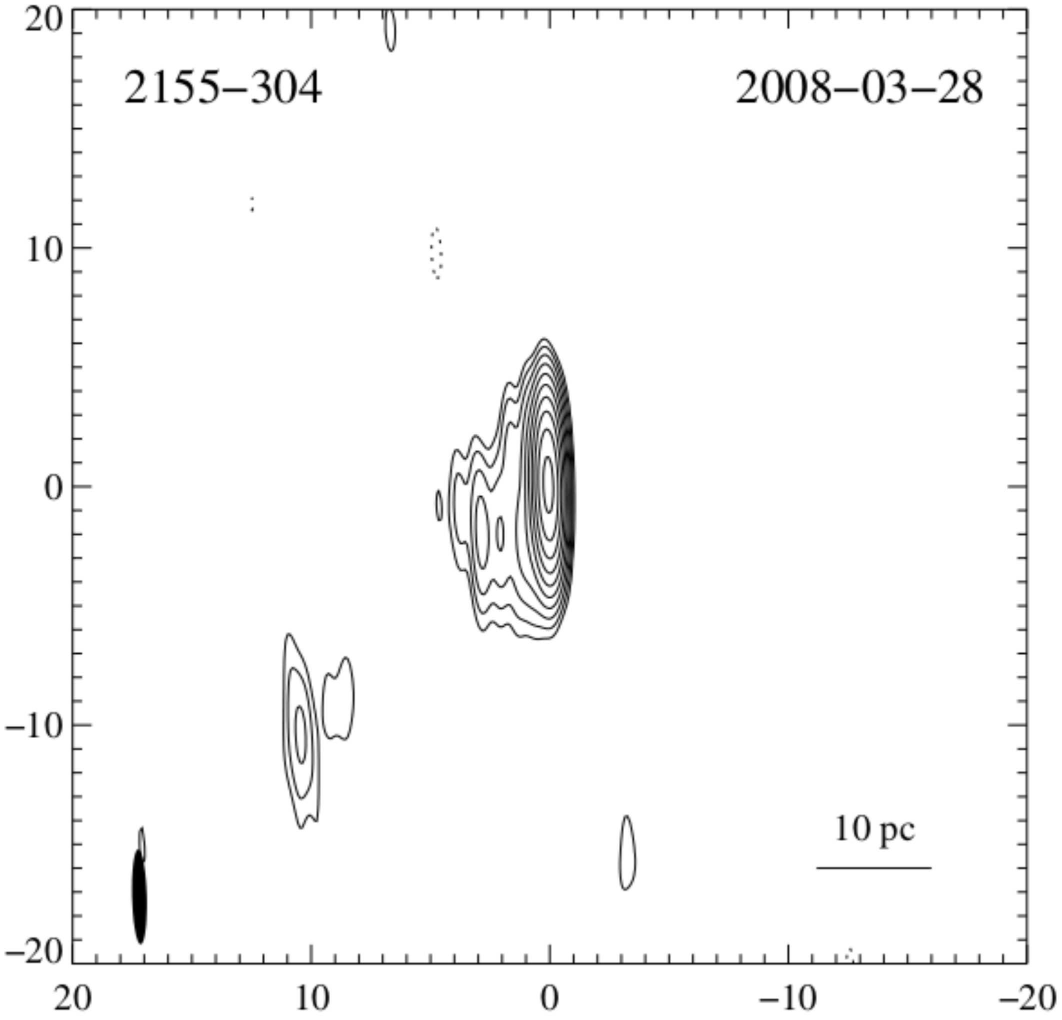

FIGURE 4.4: VLBI-image by the TANAMI-project. Showing the inner part of the AGN at parsec scales. In this image a jet emission is shown at 8.4 GHz resolved by a beam-size of (3.98 × 0.62) milliarcsec, stretching out to the South-East, the opposite direction of the actual jet in the 1.4 GHz image of the GMRT observation.

the model of a flat spectrum for Blazars due to core dominants which is here case. The lower frequency at 74 MHz the data-point by the VLA in the plotted spectrum indicates a steepening in the flux together with the flux estimated out of the radio light curve from the study of Pandey-Pommier et al. (2016) at 610 MHz. The difference of the images by Pandey-Pommier et al. (2016) and this GMRT-image although is startling, because one would expect at first a structure resembling the images of the lower frequencies. To understand why we only see one jet at 1.4 GHz it is necessary to look at other observations. A Very Long Basline Interferometry (VLBI) study was released by Ojha et al. (2010) of objects on the southern hemisphere, including PKS 2155−304. Fig. 4.4 shows the released image. With the now very long baselines a resolution of (3.98 × 0.62) milliarcsec can be obtained and the near vicinity of the core shown. Again a jet structure can be

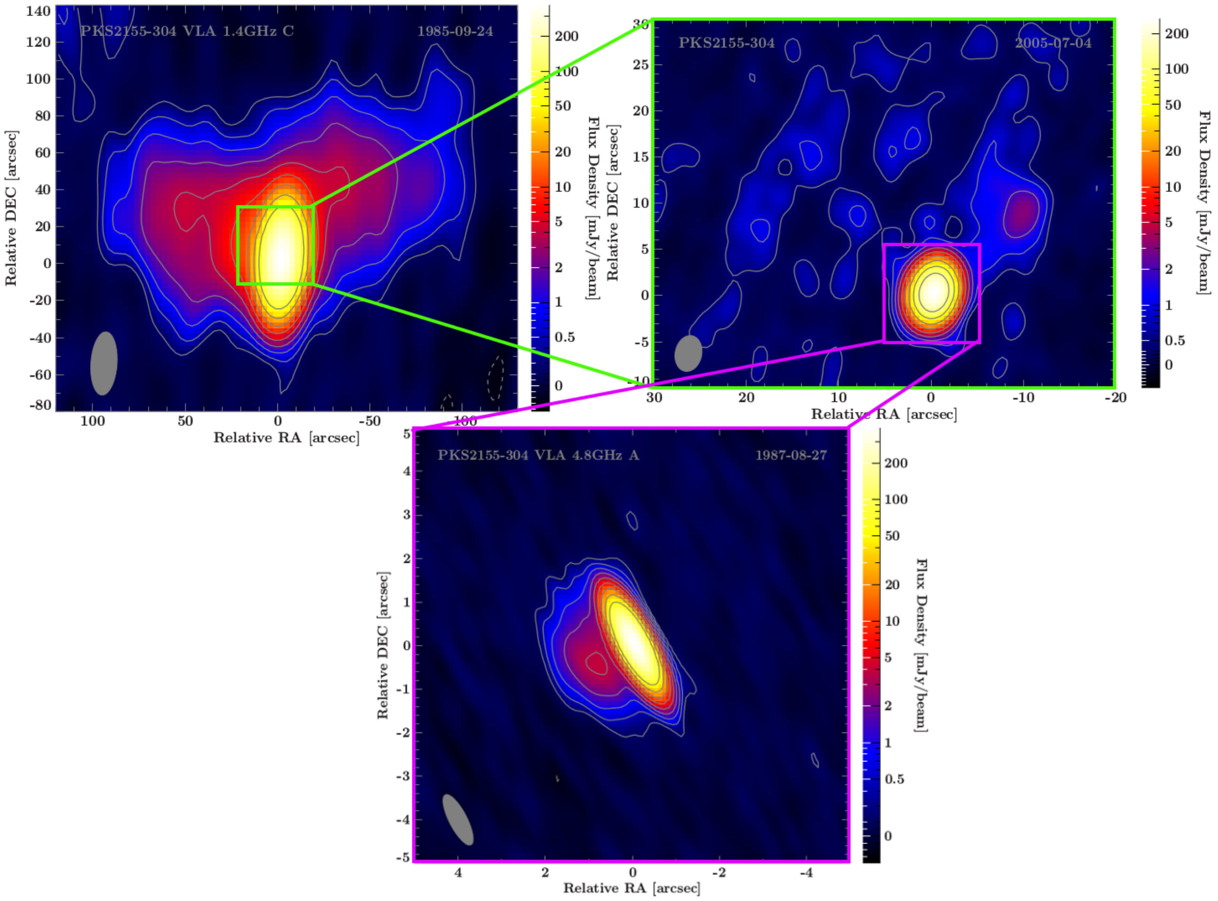

FIGURE 4.5: Comparison of different images of PKS 2155−304. Top-left: 1.4 GHz observation from the VLA at C-configuration (most compact array). Extended emission to North-Western and Eastern direction. Top-right: Zoomed in images of GMRT-data at 1.4 GHz. Bottom: VLA-image at 4.8 GHz and A-configuration (longest baseline) with only a jet structure to the South-East. From Ringholz (2017)

seen, but to the opposite direction as in the lower frequency of the GMRT-image and at much smaller scales of about 10 parsec for 5 milliarcsec. Instead the expansion of the Blazar PKS 2155−304 after Wright (2006) with the redshift z=0.116 (Falomo et al. 1993) and the cosmological model provided by the NED-database ($\Omega_{\mathrm{M}} = 0.27$, $\Omega_{\mathrm{vac}} = 0.73$, $H_0 = 0.73$ km/s/Mpc) results in 2.020 kpc per arcsec. The jet structure in the 1.4 GHz image of the GMRT would therefore expand up to ≈22.220 kpc to the North-West. The only way to explain the different jet directions in the different wavelengths and array configurations, is jet-bending. According to the unification scheme, BL Lacs are the beamed and rotated counterparts of FR1 radio galaxies, whereas quasars correspond to FR2 galaxies. Therefore a jet structure with a wider opening angle and no hot spots are expected. To now verify the suggestion of a bended structure the information of images of another array is helpful. The VLA observations, presented by (Ringholz 2017), at 1.4 GHz and 4.8 GHz in fig. 4.5 provide more evidence. Actually a comparison of images and zoomed in view of the source can be given and shows at different frequencies and

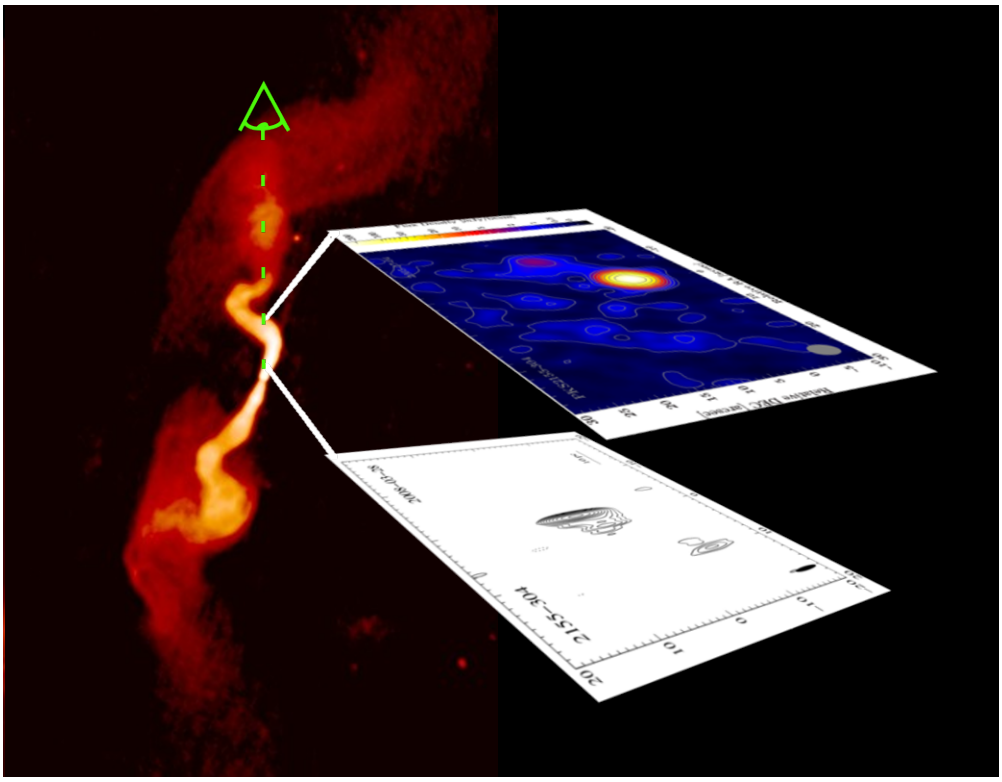

Figure 4.6: The bended structure of PKS 2155−304 in respect to the model FR1 radio AGN 3C31 (from: http://www.cv.nrao.edu/). If the view on 3C31 was pole on, the same images as for PKS 2155−304 could be seen. This clearly shows that a jet crossing the line of sight is highly possible for this source and would agree with the unified model of BL Lacs as FR1 galaxies.

beam sizes all the three situations of beam structures. The image on the top left shows what the VLA with a big collecting area can resolve, in this C-configuration with small baselines it is more sensitive to extended emission with lower resolution of (26 × 10) arcsec, but shows two jets in the same direction as in the data (Pandey-Pommier et al. 2016) provided. With higher resolution a zoomed in view of the core region can be shown with the GMRT-data and only one jet. The same holds for the 4.8 GHz image of the VLA with a much higher resolution at A-configuration due to longer baselines and higher frequency but with a jet opposite of the GMRT-image like it was seen in the VLBI-image of (Ojha et al. 2010). It can be seen that the jet emission is shifting from North-West to South-East to emit from a different direction the higher the frequency is and the higher the frequency a better look at the core near structures can be achieved. So with higher frequencies regions at higher energies are observed and this would also show that the more collimated areas, where the jet is optically thick, near the core are observed. Studies of opening angles of jet structures, like Parma et al. (1987), are therefore also important to cross check the observations of AGN but for Blazars this harder to do. These structures can be important to constrain the distances of core and jets seen

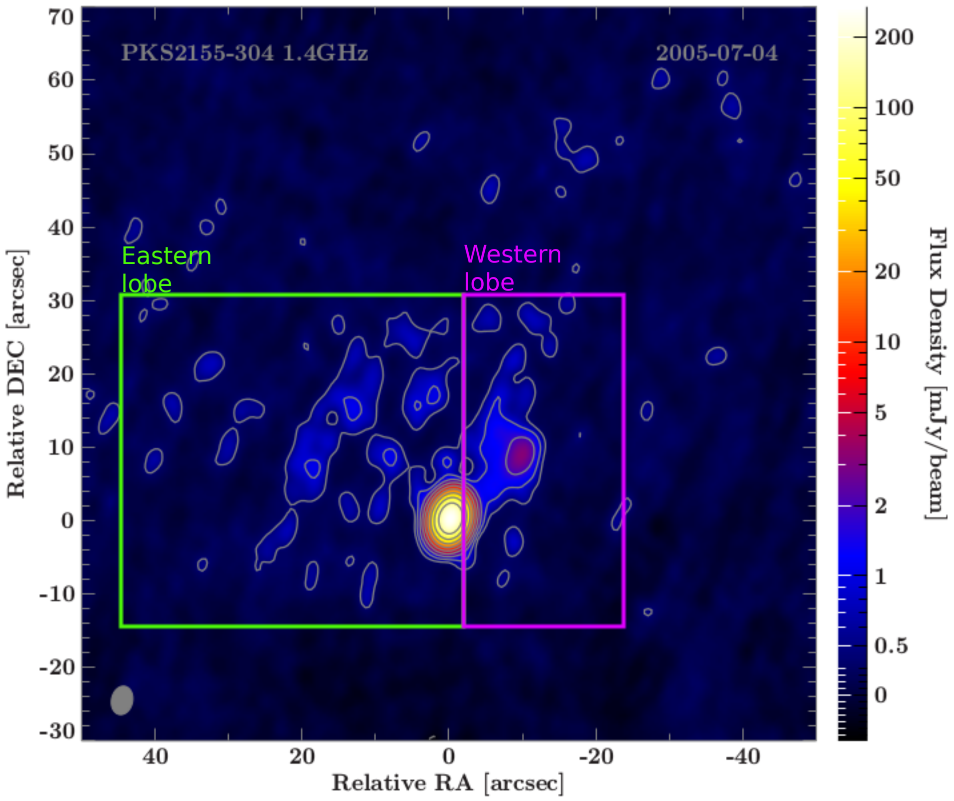

FIGURE 4.7: The 1.4 GHz image of the GMRT with both lobes indicated by the green an magenta boxes. Green would therefore show part of the counter-lobe emerging away from the observer and the magenta box is the part of jet and lobe directed towards us.

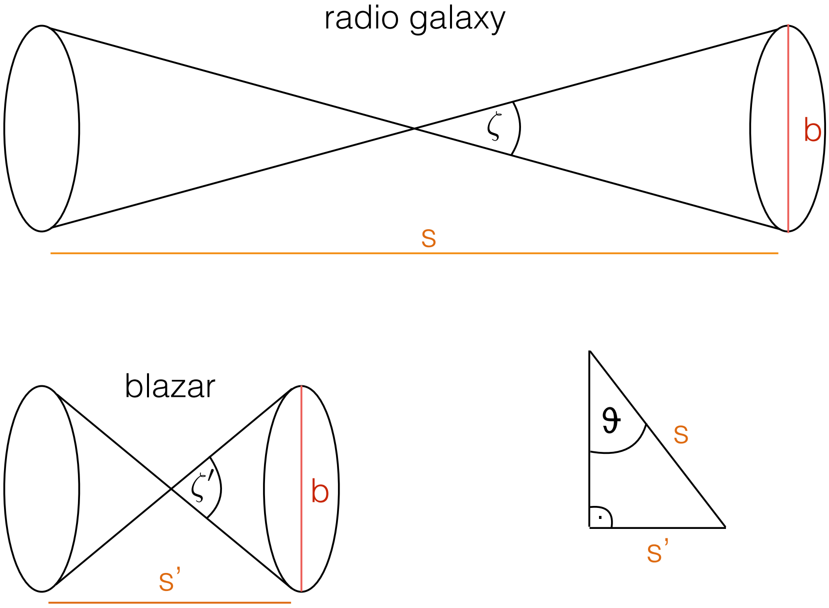

FIGURE 4.8: The model of jet cones from Burd (2017). With this model the apparent inclination angle can be constrained and a upper limit set.

in fig. 4. But for now there is striking evidence for an actually bended jet, crossing the line of sight, modelled as in fig. 4.6. The images are rotated to fit the FR1 model galaxy 3C31 from (Laing et al. 2008), and therefore the unified model can be supported with respect to the reference of BL Lac being FR1 type AGN objects. The image at 4.8 GHz of the VLA can also be sorted between the 8.4 GHz one of VLBI and 1.4 GHz GMRT one for an idea farther away from the core as the VLBI image. All in all the 3 images fit well to the model of an FR1 galaxy, especially if rotated accordingly to the 3C31 galaxy. Laing & Bridle (2002) referred to the cause of a jet bended at kilo-parsec scales by the domination of intrinsic environmental asymmetries therefore interaction with the surrounding intergalactic medium. A possibility would be a thicker intergalactic medium in its direction leading to this bended jet, even intergalactic winds (Veilleux et al. 2005). Near the core at about 1 kpc the jet is decelerated and the opening angle is higher but with low frequency observations the outer part of the jet is observed, were the jet is already decelerated and more collimated (Laing et al. 2008). Dependent on which way the jet already was influenced and bended, the 1.4 GHz image should show exactly the area after deceleration but where the jet is still collimated. At higher distances from the core a more diffuse jet is to be expected as seen in fig. 4.1 at 610 MHz to the North-West, where the jet is even more fanned out and the extended emission covers a much larger area. Also the diffuse emission emerging to the East in the 1.4 GHz image could show the counter-lobe seen in the lower frequencies, therefore both lobes can be seen as well in this image and are shown in fig. 4.7. After categorizing PKS 2155−304 to the equivalent source of a FR1 radio galaxy, the work of Burd (2017) on opening angles of a sample from Parma et al. (1987) can be applied. With the most probable intrinsic jet opening angle $\zeta_{\mathrm{mp}} = 10.9^\circ$, the model of jet cones and the opening angle of the projected AGN the probable inclination angle to the line of sight can be derived. The minimal and maximal limit for the opening angle, $\zeta_{\mathrm{min}} = 3.4^\circ$ and $\zeta_{\mathrm{max}} = 33.4^\circ$, can present a limit to the inclination angle to the jet. The problem to derive an inclination angle of the object itself in reference to the jet pointing lies in the structure of the jet itself. Near the core a greater opening angle is expected until the jet is decelerated. The perfect point of the jet for a measurement of the opening angle should be here, because afterwards, due to the collimation, the jet expands slower. The farther away from the core a smaller opening angle would then be measured if the model of Burd (2017) is applied. Fig. 4.8 shows the model, which leads to the equation of an inclination angle by a geometric approach. After it the inclination angle ϑ would be,

$$\vartheta = \arcsin\left(\frac{s'}{s}\right) = \arcsin\left(\frac{\tan\frac{\zeta}{2}}{\tan\frac{\zeta'}{2}}\right), \tag{4.1}$$

with ζ as de-projected opening angle and ζ' as projected, measured, opening angle, but would provide only a way of a vague idea to the inclination angle. Still, in the image of

	$\zeta/^\circ$	$\zeta\prime/^\circ$	$\vartheta/^\circ$	length / kpc
1	3.4	16.4	11.9	182.8
2	3.4	22.5	8.6	254.8
Mean	3.4	19.5	10.0	218.7
3	10.9	16.4	11.9	41.4
4	10.9	22.5	28.6	70.4
Mean	10.9	19.5	33.8	57.4

TABLE 4.1: The projected jet opening angle of the GMRT image with Gaussian models and the values from the study of Burd (2017) combined to constrain the inclination angle of the source to the line of sight. Note that the maximum value for ζ is 33.4° but the maximal measured angle is smaller, therefore it has to be assumed that the maximal de-projected opening angle has to be smaller as well. This results in a range for the inclination angle of 8.6° to 90.0° and lengths of the jet ranging from 38.4 kpc to 254.8 kpc.

the GMRT at 1.4 GHz an inclination angle for an approximated maximal opening angle $\zeta\prime_{\mathrm{max}} = 22.54^\circ$ at a distance of 12.80 arcsec could be achieved, by deleting the model-components around the source of the image and re-imaging the jet with Gaussian model components. A second component could be placed and modelfitted at 6.82 arcsec with $\zeta\prime_{\mathrm{min}} = 16.44^\circ$. By taking the mean value of these angles the range of the inclination angle can be approximated seen in tab. 4.1. This outcome shows the significance of the data on the opening angle for this method. It highly impacts the results of the inclination angles in a matter of the same magnitude for the given values of opening angles. But it is expected that Blazars have a small inclination angle and therefore the results at the mean value of 10.9° for opening angles are not expected to be as high. More probable, with respect to the unified model, would be the values for the inclination angle for the value of 3.4° were all results are within the region of 10°. In this example after (Wright 2006), the jet structure of PKS 2155−304 ($\approx$ 19 arcsec wide) seen in the 1.4 GHz would then, dependent on the inclination angle, expand for both projected angles from 33.8 kpc up to 254.8 kpc with the most probable widths being $L_{\mathrm{mp}3.4} = 10.0$ kpc and $L_{\mathrm{mp}10.9} = 57.4$ kpc. By accounting for the value of the small opening angle only, the expanded structure of PKS 2155−304 would range from 218.7 kpc to 254.8 kpc and give a more probable estimate about the expansion of the BL Lac.

Chapter 5

Summary and Conclusion

In this thesis a new GMRT-image at 1.4 GHz of the BL Lac PKS 2155−304 is presented. Is is compared to different images of previous and ongoing work and results in the a three dimensional view of the jet structure. The jet structure in different frequencies revealed its bending and crossing of the line of sight, which then could be further interpreted in the location of the different two dimensional views of the source. Also an indication of the counter-jet, which could be observed at lower frequencies but not in images at 1.4 Ghz, could be seen. By comparing the opening angle of the jet with statistics the inclination angle could be constrained to a minimal angle, but because of a too high maximum angle of the statistics of opening angles it was not possible to constrain it to a maximum. Maybe a better sample or different technique for the statistics could lead to a better outcome and smaller constraint. With this a statistic about the expansion of blazars could connect them even more to their edge on variant of radio galaxies.

List of Figures

List of Tables

Bibliography

AIPS, In: http://www.aips.nrao.edu/index.shtml.

Antonucci R., 1993, 31, 473

Baars J.W.M., Genzel R., Pauliny-Toth I.I.K., Witzel A., 1977, 61, 99

Bridle A.H., Hough D.H., Lonsdale C.J., et al., 1994, 108, 766

Burch S.F., 1979, 187, 187

Burd P.R., 2017, In: Private communication and Masterthesis.

Chandra P., Ray A., Bhatnagar S., 2004, 612, 974

Chevalier J., Kastendieck M.A., Rieger F.M., et al., 2016, PoS ICRC2015, 829

Clark B.G., 1999, In: Taylor G.B., Carilli C.L., Perley R.A. (eds.) Synthesis Imaging in Radio Astronomy II, Vol. 180. Astronomical Society of the Pacific Conference Series, p. 1

Falomo R., Pesce J.E., Treves A., 1993, 411, L63

Fanaroff B.L., Riley J.M., 1974, 167, 31P

Fomalont E.B., Perley R.A., 1999, In: Taylor G.B., Carilli C.L., Perley R.A. (eds.) Synthesis Imaging in Radio Astronomy II, Vol. 180. Astronomical Society of the Pacific Conference Series, p. 79

H.E.S.S. CollaborationAbramowski A., Acero F., et al., 2012, 539, A149

Högbom J.A., 1974, 15, 417

Jennison R.C., 1958, 118, 276

Kellermann K.I., Sramek R., Schmidt M., et al., 1989, 98, 1195

Laing R.A., Bridle A.H., 2002, 336, 1161

Laing R.A., Bridle A.H., Parma P., et al., 2008, 386, 657

Liuzzo E., Falomo R., Treves A., et al., 2013, 145, 73

Michelson A.A., 1890, 2, 115

Napier P.J., 1999, In: Taylor G.B., Carilli C.L., Perley R.A. (eds.) Synthesis Imaging in Radio Astronomy II, Vol. 180. Astronomical Society of the Pacific Conference Series, p. 37

Ojha R., Kadler M., Böck M., et al., 2010, 519, A45

Pandey-Pommier M., Sirothia S., Chadwick P., et al., 2016, ArXiv e-prints

Parma P., Fanti C., Fanti R., et al., 1987, 181, 244

Peacock J.A., Miller L., Longair M.S., 1986, 218, 265

Perley R.A., Butler B.J., 2013, 204, 19

Peterson B.M., 1997, An Introduction to Active Galactic Nuclei

Ringholz J., 2017, In: Private communication and Masterthesis.

Romney J.D., 1999, In: Taylor G.B., Carilli C.L., Perley R.A. (eds.) Synthesis Imaging in Radio Astronomy II, Vol. 180. Astronomical Society of the Pacific Conference Series, p. 57

Sanchez D.A., Giebels B., Zaborov D., et al., 2015, ArXiv e-prints

Scaife A.M.M., Heald G.H., 2012, 423, L30

Shakura N.I., Sunyaev R.A., 1973, 24, 337

Shepherd M.C., 1997, In: Hunt G., Payne H. (eds.) Astronomical Data Analysis Software and Systems VI, Vol. 125. Astronomical Society of the Pacific Conference Series, p. 77

Taylor G.B., Carilli C.L., Perley R.A., (eds.) 1999, Synthesis Imaging in Radio Astronomy II, Vol. 180 of *Astronomical Society of the Pacific Conference Series*, Astronomical Society of the Pacific Conference Series

Thompson A.R., 1999, In: Taylor G.B., Carilli C.L., Perley R.A. (eds.) Synthesis Imaging in Radio Astronomy II, Vol. 180. Astronomical Society of the Pacific Conference Series, p. 11

Urry C.M., Padovani P., 1995, 107, 803

Veilleux S., Cecil G., Bland-Hawthorn J., 2005, 43, 769

Wright E.L., 2006, 118, 1711

Acknowledgements

Here I would like to represent my gratitude to those giving me the strength and durability to finally arrive at one set goal on my journey to science.
I thank Prof. Dr. Matthias Kadler for giving me the chance to write this thesis and the opportunity to experience the work with data from telescopes and especially the analysing of the finalized image. Whenever I had new data to show he pointed me to new possibilities at which way to interpret the data , which resulted in great discussions and finding yet another aspect I could evolve to and to learn even more about radio-astrophysics. He also gave me the opportunity to present my results at the IWBS conference which helped greatly in finalizing this thesis.
I thank Paul Ray Burd for giving me the foundation for the work with the programs AIPS to calibrate the data and DIFMAP to image it, which were crucial for my thesis. He always provided me with all the information I needed and always had an answer to all my questions even before I started my thesis.
Also I thank Jonas Ringholz for the support while calibrating, especially in the beginning of my work. His working on VLA-data also resulted in good discussions.
I thank Tobias Beuchert, who provided me with additional information about the source PKS 2155−304.
This research has made use of ISIS functions provided by ECAP/Remeis observatory and MIT (http://www.sternwarte.uni-erlangen.de/isis/).
Also the Extragalaxtic Database (NED) of NASA/IPAC was used in this research which is operated by the Jet Propulsion Laboratory, California Institute of Technology, under contract with the National Aeronautics and Space Administration.
For always believing in me and raising me to who I am today I would like to thank my Family. My dad Volker, who always gave me something I wanted to surpass to get better in everything I did. My mother Dagmar who always is a person of tranquillity and showed me how to appreciate life in the fullest. My brother Andreas who is a never ending source of information, fun and always has a distraction if needed.
In the end I would like to thank my love Stefanie for always supporting me in every way. In the stressful time as well as in the good times she really showed me, how great life can be. Thank you my dear.

Michael Seeg

Declaration of Authorship

I, Michael Seeg, declare that this thesis titled, 'An approach to the 3D-Morphology of PKS 2155−304 on parsec to kilo-parsec scale' and the work presented in it are my own. I confirm that:

- This work was done wholly or mainly while in candidature for a research degree at this University.
- Where any part of this thesis has previously been submitted for a degree or any other qualification at this University or any other institution, this has been clearly stated.
- Where I have consulted the published work of others, this is always clearly attributed.
- Where I have quoted from the work of others, the source is always given. With the exception of such quotations, this thesis is entirely my own work.
- I have acknowledged all main sources of help.
- Where the thesis is based on work done by myself jointly with others, I have made clear exactly what was done by others and what I have contributed myself.

Signed:

Date: